Inter-valence-band hole-hole scattering in cubic semiconductors

M. V. Dolguikh, A. V. Muravjov,* and R. E. Peale†
Department of Physics and College of Optics & Photonics, University of Central Florida, Orlando, Florida 32816, USA
(Received 22 August 2005; published 27 February 2006)

Transitions between valence subbands resulting from hole-hole scattering in cubic semiconductors have been analyzed in the frame of Coulomb interaction of valence electrons in the Luttinger-Kohn representation. Expressions for transition rates are derived. Calculated rates for transitions between light- and heavy-hole bands are presented for germanium. Hole-hole scattering has remarkably different transition probabilities and scattering-angle dependence than for scattering of holes on ionized impurities. These results are particularly important for hole lifetimes and relative subband populations in unipolar *p*-type devices, such as the hot hole *p*-Ge laser. Features of hole-hole scattering for spin polarized hole distributions are also discussed.

DOI: 10.1103/PhysRevB.73.075327 PACS number(s): 72.20.Dp, 72.25.Rb, 72.25.Dc

INTRODUCTION

In semiconductors, inter-valence-band (IVB) transitions (e.g., transitions between light and heavy subbands of the valence band) caused by hole-hole scattering are important for applications where relative subband populations matter. For example, hole-hole scattering affects inversion population between light and heavy subbands in the terahertz hot-hole *p*-Ge laser,[1–3] and it is the dominant scattering process responsible for light-hole lifetime in proposed[4] multilayer δ-doped *p*-Ge laser structures. Previous Monte Carlo simulations of hole dynamics in bulk *p*-type semiconductors (particularly germanium) treated hole-hole interaction the same as scattering on impurities, whose effective concentration was taken as the sum of acceptor and mobile carrier concentrations.[1,5] This paper develops a more accurate approach.

Electron-electron and electron-hole scattering in homogeneous semiconductors has been treated previously in the center of mass coordinate system.[6–8] This approach is unsuitable for hole-hole scattering that results in IVB transitions. Intersubband carrier-carrier scattering in semiconductor quantum wells has been considered,[9–12] but results for quantum wells, where the valence band structure and hole wave functions are strongly modified by confinement, cannot be applied to bulk semiconductors. In this paper we derive rates for hole-hole scattering in bulk cubic semiconductors using explicit hole wave functions in Luttinger-Kohn representation.[13,14] This approach is especially important for accurate treatment of *inter*-valence-band transitions caused by hole-hole scattering. To illustrate some features of hole-hole scattering, calculation results for IVB light-to-heavy and heavy-to-light hole transition rates for germanium are presented.

THEORETICAL METHODS

Spin-orbit coupling splits the sixfold degenerate valence band at hole wave vector $\vec{k}=0$ for semiconductors with diamond or zinc-blende structure into a fourfold degenerate band (light and heavy subbands) and a twofold degenerate band (split-off band), which is shifted toward higher-hole energy. If both spin-orbit splitting at $\vec{k}=0$ and hole kinetic energy are small compared to the fundamental band gap, the wave functions of light- and heavy-hole states, to lowest order in k, can be written as[13]

$$\psi^{\nu}(\vec{k},\vec{r}) = \exp(i\vec{k}\cdot\vec{r}) \sum_{J=3/2,1/2} \sum_{m_J=-J}^{J} c^{\nu}_{J,m_J}(\vec{k})\psi^{J}_{m_J}(\vec{r}). \quad (1)$$

Here, ν denotes the hole subband state. The $\psi^{J}_{m_J}$ are basis functions in the Luttinger-Kohn representation[13,14] given by

$$\psi^{3/2}_{3/2} = \frac{1}{\sqrt{2}}(X+iY)\alpha, \quad \psi^{3/2}_{1/2} = \frac{i}{\sqrt{6}}[(X+iY)\beta - 2Z\alpha],$$

$$\psi^{3/2}_{-1/2} = \frac{1}{\sqrt{6}}[(X-iY)\alpha + 2Z\beta], \quad \psi^{3/2}_{-3/2} = \frac{i}{\sqrt{2}}(X-iY)\beta,$$

$$\psi^{1/2}_{1/2} = \frac{1}{\sqrt{3}}[(X+iY)\beta + Z\alpha], \quad \psi^{1/2}_{-1/2} = \frac{i}{\sqrt{3}}[-(X-iY)\alpha + Z\beta], \quad (2)$$

where X, Y, Z are the Bloch functions for $\vec{k}=0$ that transform under operations of the cubic group as Cartesian coordinates x,y,z, respectively.[13] The α and β are the spin functions corresponding to positive and negative spin projections, respectively. The spin-orbit interaction operator is diagonal in this representation, and the coefficients c^{ν}_{J,m_J} are eigenvectors of the Hamiltonian matrix.[13]

For the Coulomb interaction potential with usual exponential screening factor, the transition probability for the $\vec{k}_1+\vec{k}_2 \Rightarrow \vec{k}_3+\vec{k}_4$ process is

$$P_{1,2\to3,4}(\vec{k}_1,\vec{k}_2,\vec{k}_3,\vec{k}_4,\nu_1,\nu_2,\nu_3,\nu_4) = \frac{2\pi}{\hbar}\left|\langle\Psi_{3,4}|\frac{e^2\exp(-\beta_s|\vec{r}_1-\vec{r}_2|)}{4\pi\varepsilon_r\varepsilon_0|\vec{r}_1-\vec{r}_2|}|\Psi_{1,2}\rangle\right|^2 \times \delta(E_1+E_2-E_3-E_4), \quad (3)$$

where $\vec{k}_i$, hole wave vector; $\hbar$, Planck constant; e, electron charge; β_s, screening parameter; ε_r, relative permittivity; ε_0, permittivity of free space; and E_i, hole kinetic energy. The symmetrized two-particle states $\Psi_{i,j}$ calculated using single

hole wave functions in the ν_ith and ν_jth states are

$$\Psi_{i,j}(\vec{k}_i,\vec{k}_j,\vec{r}_i,\vec{r}_j,\nu_i,\nu_j) = \frac{1}{\sqrt{2}}\{\psi_{\nu_i}(\vec{k}_i,\vec{r}_i)\psi_{\nu_j}(\vec{k}_j,\vec{r}_j) - \psi_{\nu_i}(\vec{k}_i,\vec{r}_j)\psi_{\nu_j}(\vec{k}_j,\vec{r}_i)\}. \quad (4)$$

Using expansion (1), the initial and final two-hole states can be written as

$$\Psi_{1,2} = \frac{1}{\sqrt{2}}\sum_{i=1}^{6}\sum_{j=1}^{6} a_{ij}[\psi_i^{\mathrm{LK}}(\vec{r}_1)\psi_j^{\mathrm{LK}}(\vec{r}_2)\exp(i\vec{k}_1\cdot\vec{r}_1 + i\vec{k}_2\cdot\vec{r}_2) - \psi_i^{\mathrm{LK}}(\vec{r}_2)\psi_j^{\mathrm{LK}}(\vec{r}_1)\exp(i\vec{k}_1\cdot\vec{r}_2 + i\vec{k}_2\cdot\vec{r}_1)], \quad (5)$$

$$\Psi_{3,4} = \frac{1}{\sqrt{2}}\sum_{i=1}^{6}\sum_{j=1}^{6} b_{ij}[\psi_i^{\mathrm{LK}}(\vec{r}_1)\psi_j^{\mathrm{LK}}(\vec{r}_2)\exp(i\vec{k}_3\cdot\vec{r}_1 + i\vec{k}_4\cdot\vec{r}_2) - \psi_i^{\mathrm{LK}}(\vec{r}_2)\psi_j^{\mathrm{LK}}(\vec{r}_1)\exp(i\vec{k}_3\cdot\vec{r}_2 + i\vec{k}_4\cdot\vec{r}_1)], \quad (6)$$

where each of the indices i and j represents a pair of quantum numbers (J,m_J), and $\psi_i^{\mathrm{LK}}(\vec{r})$ are basis functions in the Luttinger-Kohn representation Eq. (2), listed as follows

$$\{\psi_i^{\mathrm{LK}}\} = \{\psi_{3/2}^{3/2},\psi_{1/2}^{3/2},\psi_{-1/2}^{3/2},\psi_{-3/2}^{3/2},\psi_{1/2}^{1/2},\psi_{-1/2}^{1/2}\}. \quad (7)$$

Matrices a_{ij} and b_{ij} are products of coefficients

$$a_{ij} = c_i^{\nu_1}(\vec{k}_1)c_j^{\nu_2}(\vec{k}_2), \quad (8)$$

$$b_{ij} = c_i^{\nu_3}(\vec{k}_3)c_j^{\nu_4}(\vec{k}_4). \quad (9)$$

Substituting Eqs. (5) and (6) into Eq. (3), using Luttinger-Kohn function orthonormality

$$\frac{1}{V_u}\int_{V_u} \psi_{m_{J_1}}^{J_1\,*}\psi_{m_{J_2}}^{J_2}\,d\vec{r} = \delta_{m_{J_1}m_{J_2}}\delta_{J_1J_2}, \quad (10)$$

(V_u, unit cell volume), and requiring momentum conservation ($\vec{k}_1+\vec{k}_2=\vec{k}_3+\vec{k}_4$) gives

$$\langle\Psi_{3,4}|\frac{e^2\exp(-\beta_s|\vec{r}_1-\vec{r}_2|)}{4\pi\varepsilon_r\varepsilon_0|\vec{r}_1-\vec{r}_2|}|\Psi_{1,2}\rangle = \frac{F_+e^2}{V_c\varepsilon_r\varepsilon_0(|\vec{k}_1-\vec{k}_3|^2+\beta_s^{\,2})} - \frac{F_-e^2}{V_c\varepsilon_r\varepsilon_0(|\vec{k}_2-\vec{k}_3|^2+\beta_s^{\,2})}, \quad (11)$$

where V_c is the volume of the crystal. In Eq. (11) the factors F_+ and F_- are

$$F_+(\vec{k}_1,\vec{k}_2,\vec{k}_3,\vec{k}_4,\vec{\nu}) = \sum_{i=1}^{6}\sum_{j=1}^{6} b_{ij}^* a_{ij}, \quad (12)$$

and

$$F_-(\vec{k}_1,\vec{k}_2,\vec{k}_3,\vec{k}_4,\vec{\nu}) = \sum_{i=1}^{6}\sum_{j=1}^{6} b_{ij}^* a_{ji}, \quad (13)$$

where $\vec{\nu}=\{\nu_1,\nu_2,\nu_3,\nu_4\}$ is a set of initial and final states. That Eq. (11) consists of the difference of two terms is due to antisymmetrization of the two-hole states, Eq. (4). Derivation of Eq. (11) involves integration of the periodic parts of wave functions Eqs. (5) and (6) over a unit cell, within which the Fourier component of the Coulomb potential is considered constant, followed by a summation over unit cells. Evaluation of (11) defines the desired matrix element in the hole-hole scattering probability Eq. (3) for any initial and final states of interacting holes. Averaging over the final hole momenta and multiplying by the total number of holes in the crystal $N=pV_c$ gives the scattering rate

$$R_{1,2\to3,4}(\vec{k}_1,\vec{k}_2,\vec{\nu}) = \frac{e^4p}{4\pi^2\varepsilon_r^2\varepsilon_0^2\hbar}\int W(\vec{k}_1,\vec{k}_2,\vec{k}_3,\vec{\nu})\delta[E_{\nu_1}(\vec{k}_1)+E_{\nu_2}(\vec{k}_2) - E_{\nu_3}(\vec{k}_3) - E_{\nu_4}(\vec{k}_1+\vec{k}_2-\vec{k}_3)]d\vec{k}_3, \quad (14)$$

with

$$W(\vec{k}_1,\vec{k}_2,\vec{k}_3,\vec{\nu}) = \left|\frac{F_+}{|\vec{k}_1-\vec{k}_3|^2+\beta_s^{\,2}} - \frac{F_-}{|\vec{k}_2-\vec{k}_3|^2+\beta_s^{\,2}}\right|^2. \quad (15)$$

In Eq. (14), $E_\nu(\vec{k})$ is the kinetic energy of a hole with momentum $\vec{k}$ in the νth subband (generally nonparabolic) and p is the hole concentration. Evaluation of Eq. (14) solves the problem of hole-hole inter- and intra-valence-band scattering rates in the approximation that the hole kinetic energy and spin orbit splitting are small compared to the fundamental gap.

When carrier kinetic energy is small compared to the spin-orbit splitting, the wave function Eq. (1) can be written in a reduced basis consisting of the first four Luttinger-Kohn functions with $J=3/2$, namely $\{\psi_{3/2}^{3/2},\psi_{1/2}^{3/2},\psi_{-1/2}^{3/2},\psi_{-3/2}^{3/2}\}$. In this approximation, the valence band is parabolic and constant energy surfaces in momentum space are warped spheres. Matrices Eqs. (8) and (9) and factors Eqs. (12) and (13) become functions of the direction of hole motion only, independent of the momentum magnitude.

For some cubic semiconductors, e.g., Ge and GaAs, band warping is weak, and the approximation of isotropic bands is valid for many problems. In this approximation, directionally averaged effective masses of light and heavy holes can be used, and the expansion coefficients $c_{m_J}^{\nu}$ in the simplified $J=3/2$ basis are simple functions of momentum direction

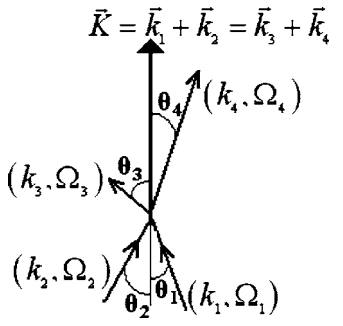

FIG. 1. Hole-hole scattering diagram.

$$c_{m_J}^{H^+}(\Omega)=\left\{ i\cos\theta e^{-i\varphi};\frac{\sqrt{3}}{2}\sin\theta;0;-\frac{1}{2}\sin\theta e^{2i\varphi}\right\},$$

$$c_{m_J}^{H^-}(\Omega)=\left\{ \frac{1}{2}\sin\theta e^{-2i\varphi};0;-\frac{\sqrt{3}}{2}\sin\theta;-i\cos\theta e^{i\varphi}\right\},$$

$$c_{m_J}^{L^+}(\Omega)=\frac{1}{\sqrt{1+3\cos^2\theta}}\left\{ i\sqrt{3}\sin\theta\cos\theta e^{-i\varphi};\right.$$
$$\left.-\frac{1}{2}(1+3\cos^2\theta);0;-\frac{\sqrt{3}}{2}\sin^2\theta e^{2i\varphi}\right\},$$

$$c_{m_J}^{L^-}(\Omega)=\frac{1}{\sqrt{1+3\cos^2\theta}}\left\{ \frac{\sqrt{3}}{2}\sin^2\theta e^{-2i\varphi};0;\frac{1}{2}(1+3\cos^2\theta);\right.$$
$$\left.-i\sqrt{3}\sin\theta\cos\theta e^{i\varphi}\right\}, \tag{16}$$

where lists are ordered according to $m_J=\frac{3}{2};\frac{1}{2};-\frac{1}{2};-\frac{3}{2}$, and (θ,φ) are polar and azimuthal angles of momentum direction, respectively. The superscripts H and L refer to heavy and light subbands, respectively. The labels "+" and "−" denoting the time-reversed pair of degenerate states in each subband may be considered as the projection of an "effective spin."

In the isotropic approximation, the energy in the νth subband is $E_\nu=\hbar^2k^2/2m_\nu^*$, where m_ν^* is the directionally averaged effective mass. The total momentum vector $\vec{k}_1+\vec{k}_2$ can be taken along the z axis as shown in Fig. 1. Then the scattering rate Eq. (14) is modified to

$$R_{1,2\to3,4}(\vec{k}_1,\vec{k}_2,\vec{\nu})=\int_0^{2\pi}\int_0^{\pi}\sin\theta_3 U(\vec{k}_1,\vec{k}_2,\vec{\nu},k_3,\theta_3,\varphi_3)d\theta_3 d\varphi_3, \tag{17}$$

where function

$$U(\vec{k}_1,\vec{k}_2,\vec{\nu},k_3,\theta_3,\varphi_3)=\frac{e^4pm_e}{4\pi^2\varepsilon_r^2\varepsilon_0^2\hbar^3}\int_0^{\infty}k_3^2D(\vec{k}_1,\vec{k}_2,\vec{\nu},k_3,\theta_3,\varphi_3)$$
$$\times\{\delta(k_3-\xi_1)+\delta(k_3-\xi_2)\}dk_3 \tag{18}$$

with

$$D(\vec{k}_1,\vec{k}_2,\vec{\nu},k_3,\theta_3,\varphi_3)=\frac{\left|\frac{F_+(\Omega_1,\Omega_2,\Omega_3,\Omega_4,\vec{\nu})}{k_1^2+k_3^2-2k_1k_3\cos\vartheta_{13}+\beta_s^2}-\frac{F(\Omega_1,\Omega_2,\Omega_3,\Omega_4,\vec{\nu})}{k_2^2+k_3^2-2k_2k_3\cos\vartheta_{23}+\beta_s^2}\right|^2}{\left[\frac{(\vec{k}_1+\vec{k}_2)^2\cos^2\theta_3}{m_4^2}-\frac{2(m_3+m_4)}{m_3m_4}\left(\frac{(\vec{k}_1+\vec{k}_2)^2}{2m_4}-\frac{k_1^2}{2m_1}-\frac{k_2^2}{2m_2}\right)\right]^{1/2}}, \tag{19}$$

and

$$\cos\vartheta_{13}=\cos\theta_1\cos\theta_3+\sin\theta_1\sin\theta_3\cos(\varphi_1-\varphi_3),$$
$$\cos\vartheta_{23}=\cos\theta_2\cos\theta_3+\sin\theta_2\sin\theta_3\cos(\varphi_2-\varphi_3). \tag{20}$$

Equation (18) defines the differential scattering rate of one of the incident holes into direction (θ_3,φ_3), with initial and final subbands of the two holes indicated by the components of $\vec{\nu}$. In Eqs. (18) and (19), $m_i=m_{\nu_i}^*/m_e$, and ξ_1, ξ_2 are the roots of the equation

$$\left(\frac{m_3+m_4}{2m_3m_4}\right)\xi^2-\left(\frac{|\vec{k}_1+\vec{k}_2|\cos\theta_3}{m_4}\right)\xi+\frac{(\vec{k}_1+\vec{k}_2)^2}{2m_4}-\frac{k_1^2}{2m_1}-\frac{k_2^2}{2m_2}=0. \tag{21}$$

Direction Ω_4, which is needed to calculate F_+ and F_-, is determined by momentum conservation. To calculate the net inter- or intra-valence-band transition rate, the rates must be summed over the effective-spin projection of the scattered holes, e.g.,

$$G(L^+,L^-;H,L)\equiv\sum_{\sigma_3,\sigma_4=+,-}R_{1,2\to3,4}(\vec{k}_1,\vec{k}_2,L^+,L^-,H^{\sigma_3},L^{\sigma_4}). \tag{22}$$

Rates (22) generally depend on the *relative* effective spin states of the incident holes in the sense that, for example

$$G(L^+,L^-;H,L)=G(L^-,L^+;H,L),$$
$$G(L^+,L^+;H,L)=G(L^-,L^-;H,L), \tag{23}$$

but

$$G(L^+,L^-;H,L)\neq G(L^+,L^+;H,L). \tag{24}$$

If the effective spin state of the hole is not of the interest, as in usual p-type devices, these rates can be averaged over effective-spin projections of the incident holes to give, for example

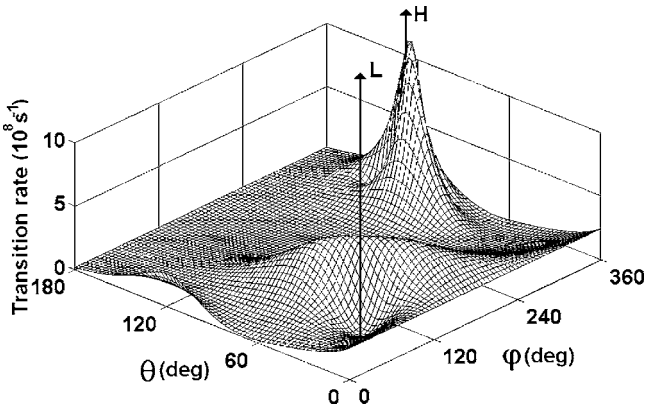

FIG. 2. Inter-valence-band differential scattering rate for the transition $LH \rightarrow HH$ as a function of final direction of one of the heavy holes. $E_1 = E_2 = 20$ meV for incident holes. Initial directions are indicated by the arrows.

$$g(L,L;H,L) \equiv \frac{1}{4} \sum_{\sigma_1,\sigma_2=+,-} G(L^{\sigma_1},L^{\sigma_2};H,L)$$

$$= \frac{1}{2} \sum_{\sigma_2=+,-} G(L^{+},L^{\sigma_2};H,L)$$

$$= \frac{1}{2} \sum_{\sigma_2=+,-} G(L^{-},L^{\sigma_2};H,L). \quad (25)$$

Due to the double degeneracy of each subband, the coefficients c^{ν}_{J,m_J} in Eq. (1) are determined not uniquely but only to a unitary transformation of the degenerate functions. Bases in each of the subbands (light and heavy) can be chosen independently of each other. Nevertheless, scattering amplitudes in a different basis can be expressed as linear superpositions of the scattering matrix elements Eq. (11) in a basis such as Eq. (16). Because of the orthogonality of wave functions with + and − effective-spin projections, scattering rates depend on the relative effective-spin projections of the interacting holes regardless of basis. Rates Eq. (25) averaged over incident effective-spin projections are independent of the choice of basis.

CALCULATION RESULTS

Calculations were performed for germanium in the approximation of isotropic and parabolic bands. In this approximation, scattering rate Eq. (17) was used. The isotropic heavy- and light-hole masses were taken to be $0.35m_e$ and $0.043m_e$, respectively.[3,7] Hole concentration was set to $p = 10^{14}$ cm^{-3}, which is typical for p-Ge lasers. At these carrier concentrations the hole gas can be considered nondegenerate, i.e., all possible final states in a scattering process are unoccupied. In general, occupation factors describing final state populations could be included. The screening parameter β_s in Eq. (19) was chosen to be 10^5 cm^{-1}, which is comparable with the average inverse distance between scattering centers at 10^{14} cm^{-3} hole concentration, though the results depend only weakly on this choice.

Figure 2 presents calculated differential rate Eq. (18) for

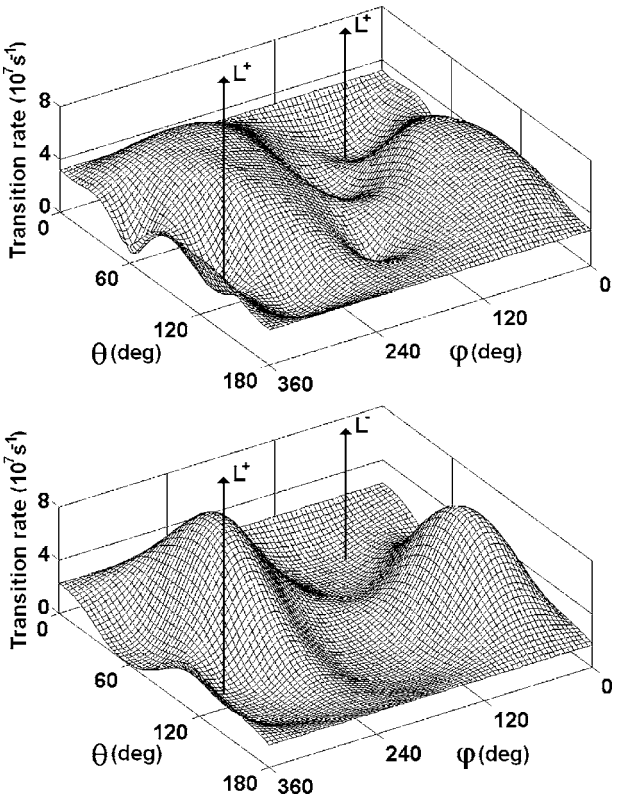

FIG. 3. Inter-valence-band differential scattering rates for the transitions $L^+L^+ \rightarrow HH$ (upper) and $L^+L^- \rightarrow HH$ (lower) as a function of final direction of one of the heavy holes. $E_1 = E_2 = 20$ meV for incident holes. Initial directions are indicated by the arrows.

IVB scattering of a light hole on heavy holes (with concentration 10^{14} cm^{-3}) as a function of final wave vector direction for one of the scattered heavy holes in terms of polar and azimuthal angles (θ_3, φ_3) (see Fig. 1). Each hole was given initial energy of 20 meV. The rate was calculated by summing over final effective-spin projections as in Eq. (22) and averaging over initial effective-spin projections of the holes as in Eq. (25). Initial directions (θ_1, φ_1) and (θ_2, φ_2) of light and heavy holes are indicated by arrows. The wave vector direction of the second scattered heavy hole (θ_4, φ_4) can be found from momentum conservation. The scattering rate is symmetric with respect to permutation of the two final heavy holes since they are indistinguishable. As expected, the IVB transition rate is sharply peaked near the direction of the incident heavy hole, which carries most of the initial momentum of the system of two interacting holes.

Figure 3 shows calculated IVB scattering rates for the collision of a single light hole on light holes with density of 10^{14} cm^{-3}. The differential rates Eq. (18) for $L^+L^+ \rightarrow HH$ and $L^+L^- \rightarrow HH$ processes, summed over final effective-spin projections as in Eq. (22), are plotted separately as a function of the final direction of one of the heavy holes (θ_3, φ_3). Arrows indicate the direction angles of the two incident light holes. Initial kinetic energy for each light hole was chosen to be 20 meV. The two plots for the different relative effective-spin projections of the incident light holes are clearly different, but generally the IVB transition rate is largest when there is a large change in momentum direction between in-

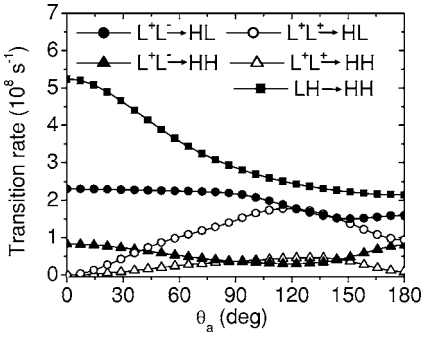

FIG. 4. Light-to-heavy hole transition rates for specific incident-hole effective-spin projections as a function of the angle of approach θ_a. $E_1=E_2=20$ meV initially.

cident light holes and the scattered heavy hole. Comparison with Fig. 2 shows that the angular dependence of IVB transition probabilities is strongly different in case of $LL\rightarrow HH$ collisions compared to $LH\rightarrow HH$ collisions.

Equation (18) integrated over final directions according to Eq. (17) determines the IVB transition rate as a function of the angle of approach $\theta_a=\cos^{-1}(\vec{k}_1\cdot\vec{k}_2)$ and initial kinetic energies of two holes. Such rates $G(L^{\sigma_1},L^{\sigma_2};H,L)$ and $G(L^{\sigma_1},L^{\sigma_2};H,H)$ for the two distinct combinations of incident effective-spin projections $\{\sigma_1,\sigma_2\}$ are compared in Fig. 4, together with the average rate $g(L,H;H,H)$, as a function of θ_a. Initial kinetic energies were set equal to 20 meV for each colliding hole. The process $LH\rightarrow HH$ was found to produce the highest IVB transition rate for all θ_a. This rate is largest when both incident holes are traveling in the same direction, which maximizes their effective interaction time. The same observation holds for processes $L^+L^-\rightarrow HH$ and $L^+L^-\rightarrow HL$. Note that the transition rate vanishes when incident light holes have the same effective-spin projection ($L^+L^+\rightarrow HH$ and $L^+L^+\rightarrow HL$ processes) and travel in the same direction with the same kinetic energy ($E_1=E_2$). This is a consequence of the antisymmetry of the wave function Eq. (4), i.e., the matrix element Eq. (11) vanishes for such holes due to the Pauli exclusion principle. As will be demonstrated below, these rates at $\theta_a=0$ become nonzero when $E_1\neq E_2$. The curves $G(L^{\sigma_1},L^{\sigma_2};H,L)$ and $G(L^{\sigma_1},L^{\sigma_2};H,H)$ as functions of θ_a depend on the choice of the basis [coefficients in Eq. (16)], but averaged rates $g(L,L;H,L)$ and $g(L,L;H,H)$ do not.

Figure 5 plots the calculated inverse IVB scattering rates for collision of two light holes as a function of their kinetic energy difference and their angle of approach θ_a. The energy of one of the incident holes is set to 20 meV. The resonant increase observed for the inverse scattering rate in the upper part of Fig. 5 is due to the decrease in the matrix element Eq. (11) when light holes with the same effective-spin projection have similar wave vectors. An increase is still notable for $\theta_a=10°$. The lower part of Fig. 5 confirms the absence of any resonance when incident light holes have different effective spin projection.

Figure 6 presents the rate $G(L^+,L^+;H,L)$ expanded into effective-spin projection components of the scattered light hole. In general, the final state of the scattered light hole

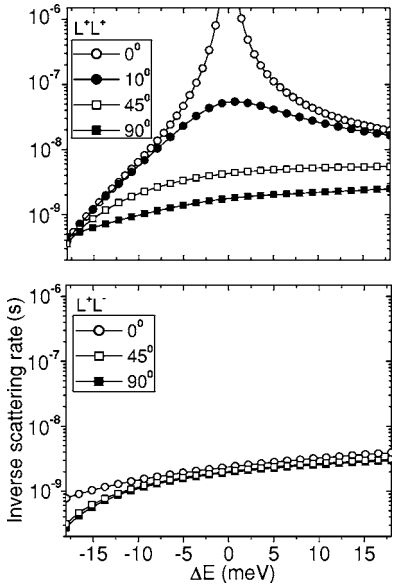

FIG. 5. Inverse inter-valence-band (light-to-heavy hole) scattering rates for collision of two light holes as a function of their kinetic-energy difference ΔE. $E_1=20$ meV, $E_2=E_1+\Delta E$, and the angle of approach θ_a is indicated in the legend. Inter-valence-band transition rates $G(L^+,L^\sigma;H,H)$ and $G(L^+,L^\sigma;H,L)$ [see Eq. (22)] are summed in the upper ($\sigma=$"+") and lower ($\sigma=$"−") figures. The upper figure includes inter-valence-band transitions that proceed via the intermediate *intra*-valence-band effective-spin-flip transitions $L^+L^+\rightarrow L^-L^+$ and $L^+L^+\rightarrow L^-L^-$.

would be a superposition of effective-spin projections. Figure 6 indicates that light holes in the $L^+L^+\rightarrow HL$ process tend to preserve their effective-spin projections. The specific dependence of scattering rate for different final state components on angle of approach depends on the choice of basis in the light subband, although the rate of transitions that flip the effective spin is always found to be smaller.

Average rates $g(L,H;H,H)$, $g(L,L;H,L)$, and $g(L,L;H,H)$ are plotted in Fig. 7 as a function of incident kinetic energies. For these calculations, the angle of approach θ_a was chosen equal to $\pi/4$. Many of the features in Fig. 7 can be understood qualitatively in terms of effective hole-hole interaction time. Transition probabilities for perturbations acting for a finite time increase monotonically with

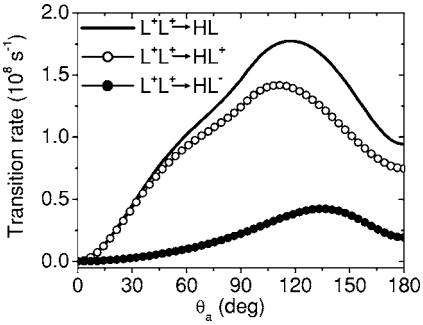

FIG. 6. $L^+L^+\rightarrow HL$ rate and its expansion into individual contributing rates for different scattered light-hole effective-spin projections. $E_1=E_2=20$ meV for incident holes.

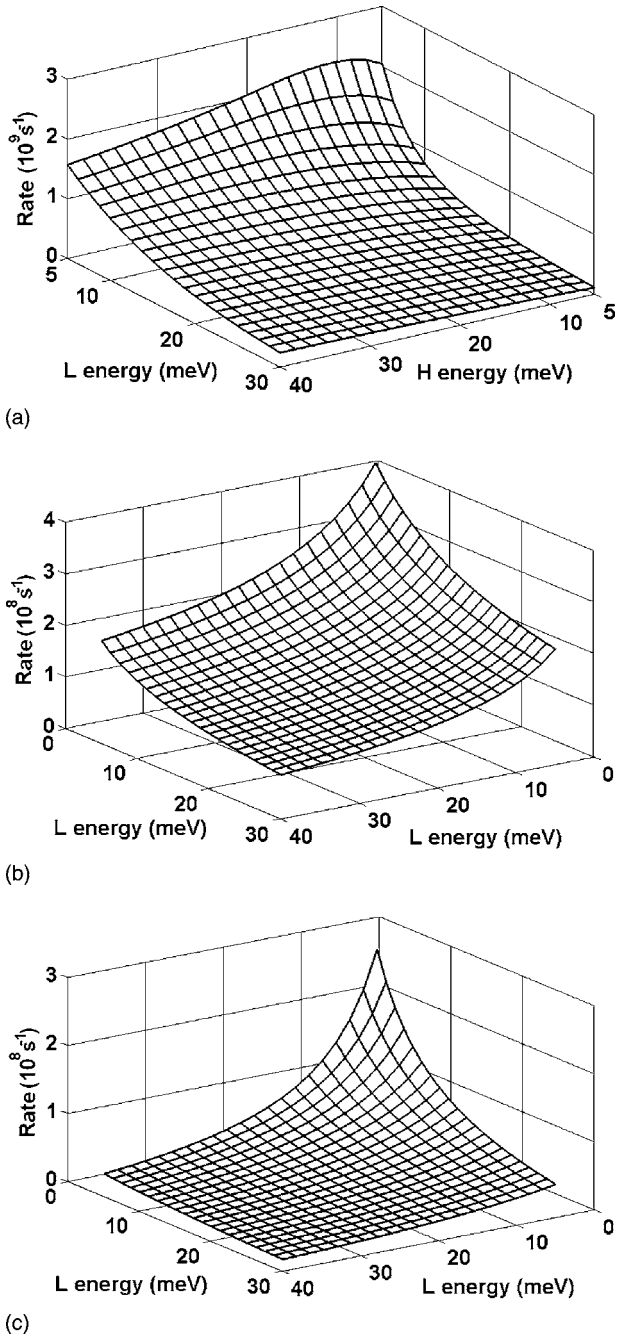

FIG. 7. Inter-valence-band $LH \rightarrow HH$ (top), $LL \rightarrow HL$ (middle), $LL \rightarrow HH$ (bottom) scattering rates vs hole kinetic energies for incident-hole angle of approach $\theta_a = \pi/4$.

the effective duration of the interaction. Thus, all rates are observed to increase as the speed of the holes decreases, which is similar to the energy dependence that occurs for impurity scattering. In the top graph, the light-hole speed is much higher than that of the heavy hole (giving small interaction time) for most of the energy range, and this explains the relatively small variation in rate with heavy-hole energy. In the middle graph, slowing either of the incident light holes has a large effect on the interaction time, and the $LL \rightarrow HL$ rate rises accordingly. For the $LL \rightarrow HH$ transitions (bottom graph) to have rates comparable to the $LL \rightarrow HL$ ones, both

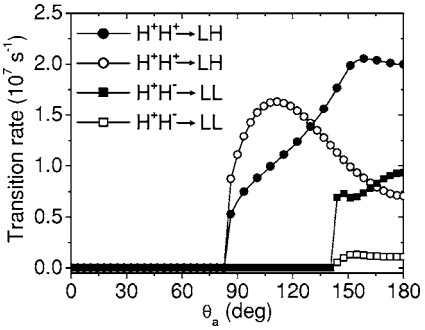

FIG. 8. Heavy-to-light inter-valence-band scattering rates for $HH \rightarrow LH$ and $HH \rightarrow LL$ processes. $E_1 = E_2 = 10$ meV for incident holes.

incident holes must be slow, because the $LL \rightarrow HH$ process has lower probability for given incident conditions (Fig. 4).

Figure 8 presents calculations of heavy-to-light hole transition rates $G(H^{\sigma_1}, H^{\sigma_2}; L, H)$ and $G(H^{\sigma_1}, H^{\sigma_2}; L, L)$ as functions of θ_a for different effective-spin projections of the incident heavy holes. Initial kinetic energy of each hole was chosen equal to 10 meV. As can be seen from Fig. 8, heavy-to-light IVB transitions have low probabilities compared with the reverse (light-to-heavy hole) process (Figs. 2–7) because of the large momentum transfer between heavy and light holes. Such transitions occur only if the two incident heavy holes have nearly opposite directions. The rate of the process $HL \rightarrow LL$ is negligibly small compared to even the $HH \rightarrow LL$ process and is not plotted here.

DISCUSSION AND CONCLUSION

Evaluation of Eq. (14) determines the scattering rate for any initial and final states of interacting holes in any cubic semiconductors where spin-orbit splitting and hole kinetic energy are small compared to the band gap. When summed over scattered, and averaged over incident, effective-spin projections [Eqs. (22) and (25)] IVB transition rates that are independent of the choice of the basis [coefficients in Eq. (1)] are determined. In the isotropic valence band approximation the rate Eq. (17) with simplified wave function expansion coefficients, Eq. (16) can be used. Example calculation of IVB transition rates, presented in Figs. 2–8, illustrate the implementation of the formulas in the simple case of isotropic valence band approximation for Ge. The curves plotted in Figs. 2–8 are virtually unchanged when the screening parameter β_s is set to zero (infinite screening length). This confirms the unimportance of a precise screening model for IVB transitions.

Among all IVB light-to-heavy hole scattering processes, scattering of light holes on heavy holes $LH \rightarrow HH$ is the strongest light-subband depopulating process (see Fig. 4). Both of the processes $LL \rightarrow HL$ and $LL \rightarrow HH$, normalized on the same scattering center concentration, give transition rates with the same order of magnitude as for the $LH \rightarrow HH$ process, but the concentration of light holes is usually much lower than the concentration of heavy ones. However, for some strongly anisotropic carrier distributions with strong

IVB inversion population, as occurs in the hot-hole *p*-Ge laser,[1–3] these processes become important and should be retained in calculations. Heavy-to-light hole scattering is ineffective (Fig. 8) and heavy holes tend to stay in their subband. Figure 7 shows that for hole-hole scattering, slow light holes have the highest IVB transition rates, which is similar to the situation for ionized impurity scattering.

Scattering rates for specific effective-spin projections depend on the choice of the coefficients in the expansion Eq. (1) for the pair of degenerate functions belonging to a given subband. In spin-polarized distributions, the coefficients would be determined by the conditions of the experiment, and the dependence of scattering on effective-spin projection would be important. In usual devices without spin polarization, rates should be averaged over incident, and summed over scattered, effective spin projections. Such rates are independent of the choice of coefficients in Eq. (1). They can be used to calculate corrections to light- and heavy-hole lifetimes in unipolar *p*-type systems, such as the *p*-Ge laser.

Because of the angular dependence illustrated in Figs. 3 and 4, hole-hole scattering rates depend on the angular part of the light- and heavy-hole distribution functions in momentum space, in contrast with ionized impurity scattering, where only the distribution over the magnitude of momentum matters in the isotropic band approximation. The more anisotropic the carrier distribution function, the more hole-hole scattering differs from ionized impurity scattering. For strongly anisotropic distribution functions, like in the hot-hole *p*-Ge laser, scattering rates and lifetimes associated with them can differ significantly from those of ionized impurity scattering,[4] and the previous approach[1,5] with doubled effective ionized impurity concentration is inaccurate. The approach presented here is especially important for situations with high local concentrations, where ionized impurity and hole-hole interactions are the main scattering mechanisms. The methods presented in this paper have been used recently in the design of *p*-Ge laser structures.[4]

ACKNOWLEDGMENTS

This work was partially supported by AFOSR Contracts No. F49620-02-C-0025 and No. F49620-02-C-0027. R.E.P. acknowledges support from ASEE/AFRL and the encouragement of Richard Soref at AFRL/SNHC Hanscom AFB, MA.

*On leave from Institute of the Physics of Microstructures, RAS, Nizhny Novgorod, Russia.

†Electronic address: rep@physics.ucf.edu

[1] V. N. Shastin, Opt. Quantum Electron. **23**, S111 (1991).

[2] E. Bründermann, in *Long Wavelength Infrared Semiconductor Lasers*, edited by H. K. Choi (Wiley, Hoboken, NJ, 2004), pp. 279–343.

[3] A. A. Andronov, A. M. Belyantsev, E. P. Dodin, V. I. Gavrilenko, Yu. L. Ivanov, V. A. Kozlov, Z. A. Krasil'nik, L. S. Mazov, A. V. Muravjov, I. M. Nefedov, V. V. Nikanorov, Yu. N. Nozdrin, S. A. Pavlov, V. N. Shastin, V. A. Valov, and Yu. B. Vasil'ev, Physica B & C **134**, 210 (1985).

[4] M. V. Dolguikh, A. V. Muravjov, R. E. Peale, M. Klimov, O. A. Kuznetsov, and E. A. Uskova, J. Appl. Phys. **98**, 023107 (2005).

[5] E. V. Starikov and P. N. Shiktorov, Opt. Quantum Electron. **23**, S177 (1991).

[6] B. K. Ridley, *Quantum Processes in Semiconductors* (Oxford University Press, New York, 1999).

[7] C. Jacoboni and L. Reggiani, Rev. Mod. Phys. **55**, 645 (1983).

[8] A. Matulionis, J. Požela, and A. Reklaitis, Solid State Commun. **16**, 1133 (1975).

[9] A. Moškova and M. Moško, Phys. Rev. B **49**, 7443 (1994).

[10] J. H. Smet, C. G. Fonstad, and Q. Hu, J. Appl. Phys. **79**, 9305 (1996).

[11] P. Kinsler, P. Harrison, and R. W. Kelsall, Phys. Rev. B **58**, 4771 (1998).

[12] Z. Ikonic, P. Harrison, and R. W. Kelsall, J. Appl. Phys. **96**, 6803 (2004).

[13] G. L. Bir and G. E. Pikus, *Symmetry and Strain-Induced Effects in Semiconductors* (Wiley, New York, 1974).

[14] J. M. Luttinger and W. Kohn, Phys. Rev. **97**, 869 (1954).